Acta Materialia 224 (2022) 117505

Contents lists available at ScienceDirect

Acta Materialia

journal homepage: www.elsevier.com/locate/actamat

In Situ TEM tensile testing of bicrystals with tailored misorientation angles

Mehrdad T Kiani[a,1], Lucia T Gan[b,1], Rachel Traylor[b], Rui Yang[b], Christopher M Barr[d], Khalid Hattar[d], Jonathan A Fan[b,*], X Wendy Gu[c,*]

[a] Department of Materials Science & Engineering, Stanford University, Palo Alto, CA, 94305, USA
[b] Department of Electrical Engineering, Stanford University, Palo Alto, CA, 94305, USA
[c] Department of Mechanical Engineering, Stanford University, Palo Alto, CA, 94305, USA
[d] Center for Integrated Nanotechnologies, Sandia National Laboratories, Albuquerque, NM, 87185, USA

ARTICLE INFO

Article history:
Received 24 June 2021
Revised 21 September 2021
Accepted 17 November 2021
Available online 24 November 2021

Keywords:
Fracture
Plasticity
Dislocations
Grain boundaries

ABSTRACT

Grain boundaries have complex structural features that influence strength, ductility and fracture in metals and alloys. Grain boundary misorientation angle has been identified as a key parameter that controls their mechanical behavior, but the effect of misorientation angle has been challenging to isolate in polycrystalline materials. Here, we describe the use of bicrystal Au thin films made using a rapid melt growth process to study deformation at a single grain boundary. Tensile testing is performed on bicrystals with different misorientation angles using *in situ* TEM, as well as on a single crystalline sample. Plastic deformation is initiated through dislocation nucleation from free surfaces. Grain boundary sliding is not observed, and failure occurs away from the grain boundary through plastic collapse in all cases. The failure behavior in these nanoscale bicrystals does not appear to depend on the misorientation angle or grain boundary energy but instead has a more complex dependence on sample surface structure and dislocation activity.

1. Introduction

Grain boundaries (GBs) are ubiquitous structural features in metals that play an important role in mechanical behavior. The effect of GBs on strength, ductility and fracture is complex, and depends on numerous structural parameters such as GB spacing, geometry, misorientation angle, atomistic structure and chemical composition, as well as proximity to microstructural features such as dislocations and precipitates [1–10]. In addition, strain rate, stress state, and temperature influence the behavior of GBs. For instance, within ductile polycrystalline metals that fail via transgranular fracture, GBs act as obstacles for crack growth, which leads to increased fracture toughness and enhanced ductility [10]. Less commonly, fracture can occur along pre-existing GBs, which is intergranular fracture. This is associated with decreased ductility of the sample and low fracture toughness [3,6]. The misorientation angle between grains has been identified as a key parameter that determines the failure mode. High angle GBs within polycrystalline samples are more susceptible to intergranular fracture due to the large lattice mismatch, high GB energy, and low cohesion strength [10].

The deformation mechanisms that lead to these failure processes such as dislocation emission from a crack tip [11] and void formation [10], are difficult to observe dynamically. The relationship between GB misorientation angle and deformation mechanism remains unclear, because this information is generally deduced from post-failure scanning and transmission electron microscopy (SEM/TEM) imaging on polycrystalline samples, which is difficult to compare to computational modeling of single grain boundaries [1,8,10,12]. Molecular dynamics (MD) simulations have shown that a higher GB energy results in easier dislocation transmission across the GB [13], such that low energy GBs (e.g. $\Sigma 3$) result in dislocation pile-up and strain hardening [13,14]. Tensile strength has been found to peak at a misorientation angle of $\sim 110^\circ$ in Cu bicrystals in MD simulation [15]. Unlike the simulated GBs, bulk polycrystalline samples contain a multitude of GBs and other microstructural features, each of which is structurally unique and subjected to slightly different loading conditions. In addition, the dynamic processes often do not

* Corresponding authors at: 452 Escondido Mall, Stanford University, Stanford, CA, 94305, USA.

E-mail addresses: mkiani@stanford.edu (M.T. Kiani), luciagan@stanford.edu (L.T. Gan), rtraylor89@gmail.com (R. Traylor), rui.yang@sjtu.edu.cn (R. Yang), cmbarr20@gmail.com (C.M. Barr), khattar@sandia.gov (K. Hattar), jonfan@stanford.edu (J.A. Fan), xwgu@stanford.edu (X. Wendy Gu).

[1] denotes equal contribution

https://doi.org/10.1016/j.actamat.2021.117505
1359-6454/

leave identifiable traces that can be used to identify deformation mechanisms.

To bridge the gap between modeling and bulk samples, experiments can be conducted on bicrystal samples that contain a single, well-characterized grain boundary. In large bicrystal samples made from fcc metals, the propensity for transgranular fracture has been correlated with the GB energy [6,16,17], whereas bcc molybdenum bicrystals show intergranular fracture for all GB angles [18,19]. More recently, focused ion beam (FIB) milled bicrystal nano- and micropillars have provided important insights on dislocation-GB interactions and GB sliding [7,20,21]. Pillar size has been observed to influence this behavior. Strain hardening occurs due to dislocation pileup for high angle GBs in microscale pillars [22–24], while strain softening is observed in sub-micron pillars [25,26]. At smaller pillar sizes, high angle GBs act as dislocation sinks and pile-up is not observed in post-deformation TEM [7,26]. In addition, GBs in >1 µm micropillars can serve as sinks, transmission, and re-emission sites for dislocations [22,24,26–28]. GBs in nanopillars serve as sinks, and dislocations are nucleated from free surfaces [26]. For GBs which are not orthogonal to the loading axis, shear stress leads to GB sliding, which has a lower activation stress than for dislocation activity [7]. Thus far, bicrystal pillars have only been tested in compression, which does not reveal tensile failure mechanisms. Nanowires [29–31] and freestanding polycrystalline metal thin films [32–40] have been tested in tension, but the mechanical response cannot be isolated at a single GB in these experiments.

Here, we investigate the *in situ* TEM tensile deformation of individual high angle grain boundaries using bicrystal Au thin films fabricated via the rapid melt growth process. These bicrystal (111)-oriented Au thin films possess a wide range of <111> tilt GB misorientation angles [41]. FIB is used to remove bicrystals from a substrate, and shape the samples into a dog-bone, after which the samples are placed on push-to-pull devices for *in situ* TEM tensile testing. Plasticity and failure of Au bicrystals with misorientation angles of 25°, 35° (close to a Σ7 GB), and 56° (close to a Σ3 twin GB) are compared to a single crystal sample. We find that failure occurs away from the GB in all cases, at tensile strengths of 300 to 675 MPa. Failure of the samples does not appear to be correlated with GB orientation or energy.

2. Materials and methods

2.1. Growth of Au bicrystals

Samples are grown according to previously published methods [41]. 600 nm of thermal oxide was grown on silicon wafers. A 30 nm thick Pt metal layer was deposited on the thermal oxide substrate through electron beam evaporation and patterned into seeds through photolithography and metal lift-off. Next, 70-100 nm of Au was deposited and patterned into wires. The Au-Pt metal structures are encased in a 3 μm thick crucible of low-pressure chemical vapor deposition (LPCVD) silicon dioxide and annealed to 1080°C in a rapid thermal annealer. After cooling, liquid phase epitaxy drives bicrystal formation. Following annealing and crystallization, the width of the Au wires decreases, and the thickness increases to roughly 150 nm. After removing the LPCVD oxide encapsulating layers through dry plasma etching, 150 nm thick Au contact pads were deposited 8-20 μm apart around each GB to anchor the Au wires for suspension. The bicrystals are suspended in air by etching the underlying thermal oxide substrate through HF vapor etching.

2.2. Characterization and in situ mechanical testing

The SEM images detailing the FIB liftout process were collected using a FEI Helios G4 UX dual-beam Focused Ion Beam Microscope. Electron backscatter diffraction (EBSD) images were collected using a FEI Strata 235DB dual-beam Focused Ion Beam Microscope equipped with an EDAX EBSD detector. The push-to-pull experiments were performed using a Hysitron PI-95 TEM PicoIndenter in a FEI TitanX 60-300 Transmission Electron Microscope and TEAM I double-aberration-corrected scanning transmission electron microscope located at the National Center for Electron Microscopy at Lawrence Berkeley National Laboratory and a 200 kV JEOL 2100 Transmission Electron Microscope at Sandia National Laboratories. Tensile testing was performed at a constant load rate of 3 to 7 µN/s. We are unable to determine strain during these experiments due to the lack of fiducial markers on the sample, which prevents us from converting the indenter tip displacement to sample displacement. Thus, the mechanical behavior of the samples is reported as stress-tip displacement curves. All movies are played back at 2x speed of test.

The indenter force and tip displacement are recorded by the TEM nanoindenter holder. The stress applied on the sample, σ, is a function of indenter force, F, and sample cross-sectional area and calculated by

$$\sigma = \frac{F}{wt}$$

where w is the width of the dog-bone and t is the sample thickness. The width and thickness dimensions were measured from TEM and SEM images. The width of the 25° bicrystal was 625 nm, the 35° bicrystal was 540 nm, and the 56° bicrystal was 540 nm. The width of the single crystal sample was 680 nm. The gauge length of all the samples was approximately 1 μm. All tested samples were approximately 140-150 nm thick.

3. Results

Fig. 1A displays an SEM image of a suspended bicrystal bisected by a single GB. The fabrication technique described in the Materials and methods section allows us to lift-out a planar, electron-transparent sample without using FIB to thin the sample in the imaging direction, which reduces FIB-induced damage. The suspended bicrystal is lifted out using a micromanipulator (Fig. 1B), welded across a 2.5 μm gap on a push-to-pull device (blue dashed region in Fig. 1C), and milled into a dog-bone shape (Fig. 1D & E). The push-to-pull device translates a compression force applied by a diamond indenter on a Hysitron PI-95 TEM PicoIndenter into a uniaxial tensile force on the sample (direction of loading is indicated by the arrows in Fig. 1E). All single crystals and bicrystals produced through this rapid melt growth are (111)-oriented normal to the substrate and result in <111> tilt GBs, which is corroborated by EBSD maps (Fig. 1F).

Three separate Au bicrystals were tested *in situ* with varying misorientation angles. The bicrystal shown in Fig. 2 has a GB misorientation angle of 35°, as determined by EBSD (Fig. 1F). The GB is perpendicular to the loading axis. Higher magnification TEM imaging of the sample shows light contrast regions of hundreds of nanometers in size, that are surrounded by darker material, on either side of the GB (Fig. 2). This contrast difference could be due to thickness variations templated from the oxide crucible [41,42]. The cellular regions of high and low contrast do not change during tensile loading and do not interact with surface-nucleated mobile dislocations (Movie S2). These regions are likely thickness variations that form during crystal growth. There is ~1 nm surface roughness along the edges of the samples due to FIB milling. Previous high resolution scanning TEM cross sections of the samples showed a

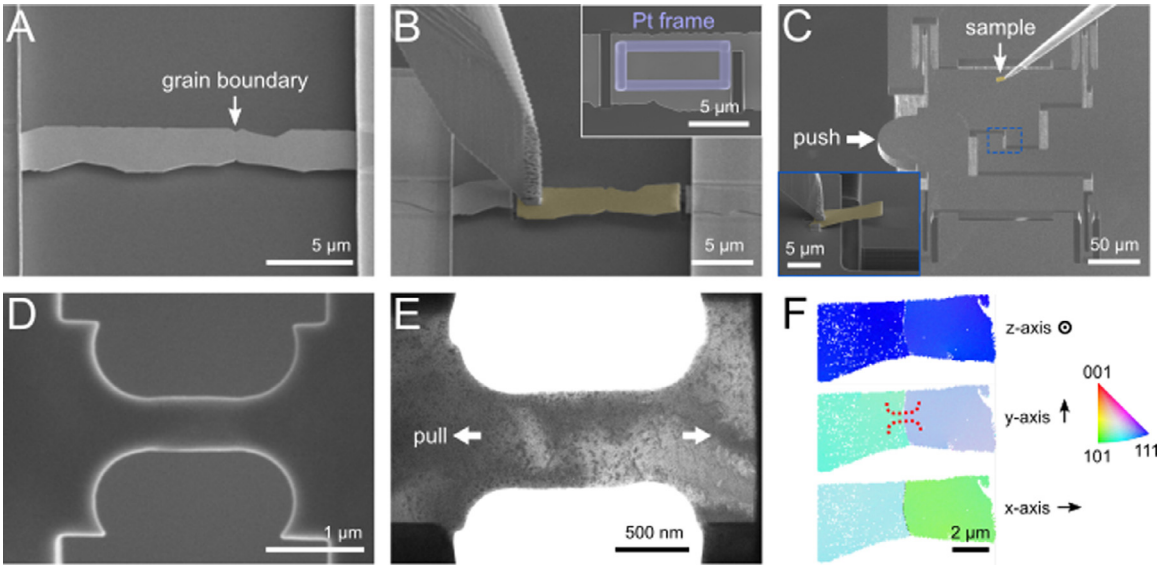

Fig. 1. Preparation of *in situ* TEM samples. A) Gold bicrystal wires are suspended in air for sample lift-out. The GB is indicated by the arrow. B) A bicrystal is detached from the chip using focused ion beam milling and lifted out with a nanomanipulator. Inset: Some of the thin-film bicrystal structures required a platinum-deposited frame to prevent bending during liftout. C) A bicrystal is mounted to a push-to-pull device in the region marked by dashed lines. The push-to-pull device translates a pushing force on the button to a tensile force on the sample. Inset: A bicrystal is welded to the push-to-pull device with platinum. D) A bicrystal is shaped into a dog-bone using focused ion beam milling. E) TEM image of a dog-bone shaped sample. The tensile force direction is indicated by the arrows. F) EBSD orientation maps of a representative bicrystal (tested in Fig. 2). All bicrystals are (111)-textured in the z-direction. The approximate location of the dog-bone shaped testing area is overlaid on the EBSD image with red dashed lines.

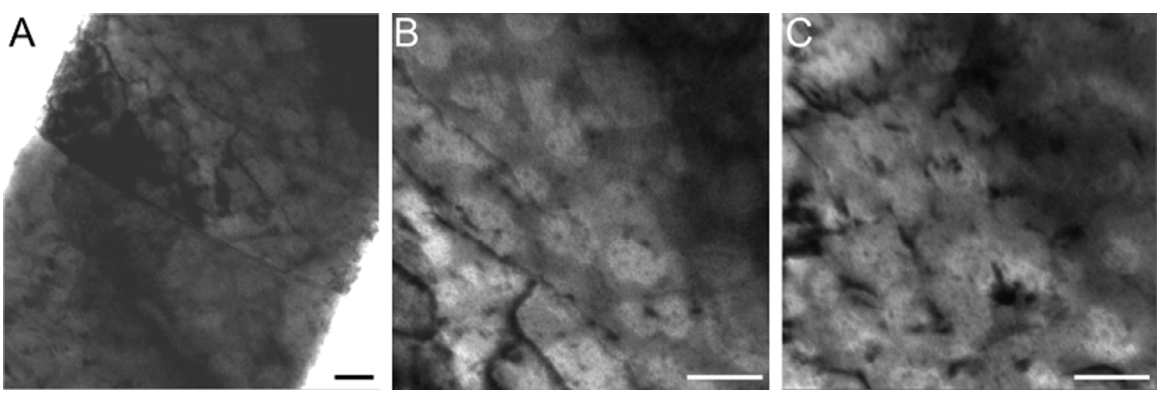

Fig. 2. Higher magnification TEM images of bicrystal in Fig. 2 showing the GB (A) and light cellular regions surrounded by dark areas on both sides of the GB (B-C). The cellular regions do not change during tensile loading and do not interact with surface-nucleated mobile dislocations. Scale bar is 50 nm.

few dislocations near the GB, but the field of view was too small to estimate dislocation density [41]. In this sample, we potentially observe dislocations within 200 nm of the GB in the upper grain, with no apparent dislocations further away. For the upper grain, there is an estimated dislocation density of 5×10^{13} m^{-2} within that region. These defects and microstructure do not appear to interact with dislocations nucleated during mechanical loading and thus do not appear to play a role in the mechanical behavior.

The stress-displacement curve for the sample is shown in Fig. 3A. Tensile testing was performed at a load rate of 5 μN/s (Movie S1). Video of the deformation was taken in bright-field (BF) TEM mode. Yielding occurred at approximately 300 MPa. Partial dislocations nucleate at the free surface in the upper grain, and propagate across the grain to form stacking faults, which can be seen as light streaks in Fig. 3B. Further loading leads to dislocation nucleation in both grains (Fig. 3C), and strain hardening in the sample. The ultimate tensile stress in the sample is 610 MPa at which point an apparent twin forms in the lower grain at the edge of the GB (Fig. 3D). The overall deformation of the sample can be described as slip that occurs in one of the grains, which leads to necking and twinning at about 45° to the loading axis. Finally, failure occurs along this low energy twin boundary and results in rapidly decreasing stress (Fig. 3E). This can be considered a type of intergranular failure, but does not occur at a pre-existing GB. We do not observe any GB sliding or motion during the test.

Two more bicrystals with 56° and 25° misorientation angles were also tested *in situ* (Fig. 4). Tensile testing was performed at a load rate of 4 μN/s and 3 μN/s, respectively (Movie S3 & S4). Videos of the deformation were taken in BF TEM mode. The 56° bicrystal had a GB perpendicular to the loading direction (Fig. 4B), while the 25° bicrystal had a curved GB which is oriented 15° from the loading direction (Fig. 4D). The GB could be tracked throughout the experiments. Dislocation motion was not visible during loading in these samples. Both bicrystals have pronounced strain hardening and no apparent twin formation. The yield strengths are also very similar at approximately 675 MPa for the 56° bicrystal and 650 MPa for the 25° bicrystal. No GB motion was observed during loading. In the 25° bicrystal, fracture occurred at the edge of the

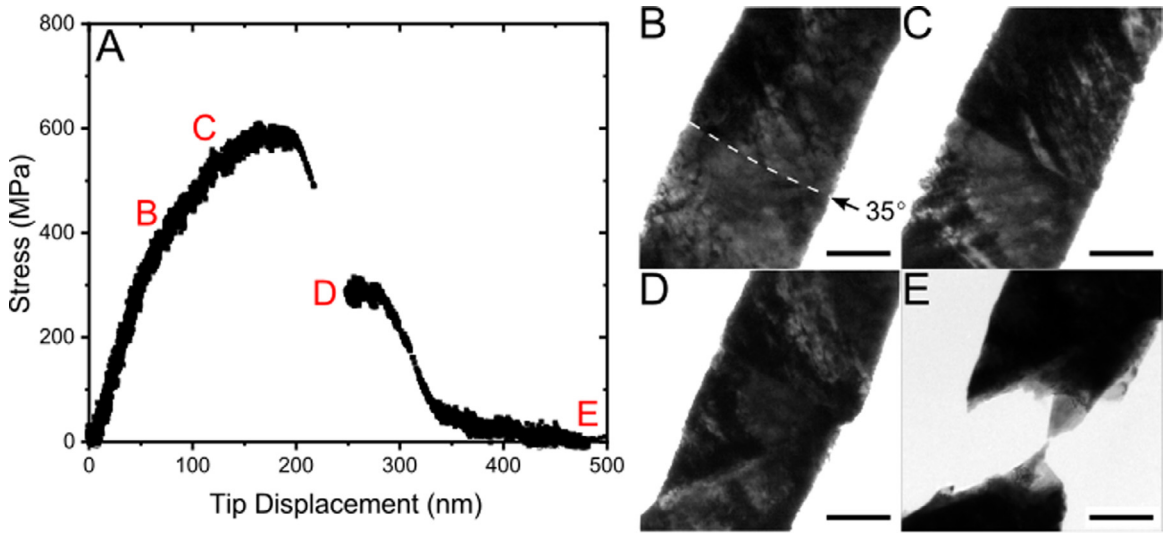

Fig. 3. A) Stress-displacement curve with corresponding TEM snapshots (B-E) at different points during the tensile test. B) Stacking faults begin to form in each grain. The GB is indicated by the black arrow and white dashed line. C) Further loading leads to continued stacking fault formation and strain hardening. D) Twin forms in lower grain at edge of GB. E) Further loading leads to ductile fracture along the twin. The contrast in B-D is increased to see stacking faults, which are streaks of light contrast. Scale bar is 200 nm.

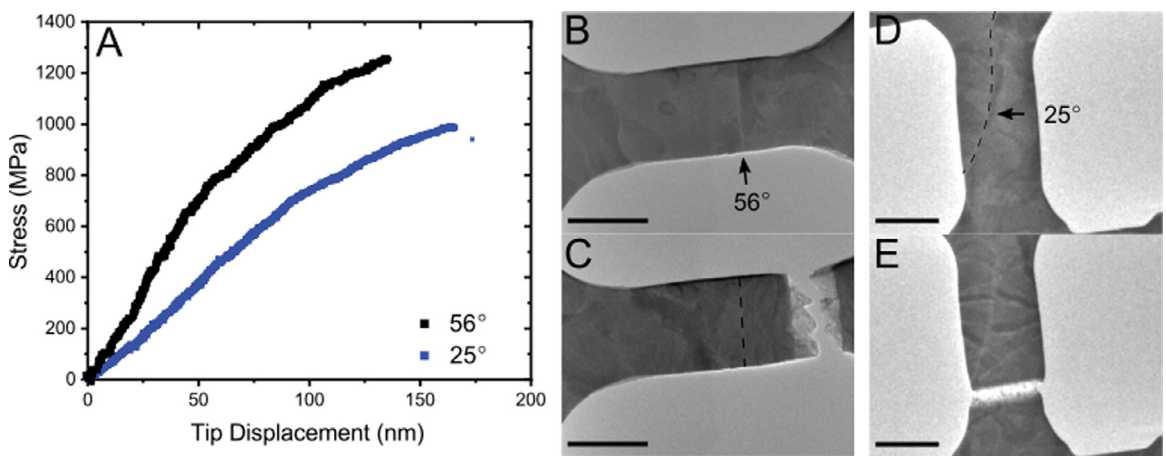

Fig. 4. A) Stress-displacement curve from a tensile test performed on gold bicrystals and the corresponding TEM images before (B, D) and after (C, E) the tensile tests. GBs are indicated by the arrows and dashed line. Scale bar is 500 nm.

GB at 990 MPa whereas fracture in the 56° bicrystal occurred away from the GB at 1250 MPa. In both cases, the fractured surface was perpendicular to the loading direction with thinned jagged edges, in contrast to the 35° bicrystal, which fractured along the twin. Fig. 5 shows EBSD maps of the thin films used to make the bicrystals in Fig. 4, and the location of the dog-bone on the as-grown thin films.

As a point of comparison for bicrystal samples, we tested a single crystal Au sample (Fig. 6) at a loading rate of 7 μN/s. Video of the deformation was taken in scanning TEM mode using a high-angle annular dark-field (HAADF) detector to observe defect motion (Movie S5). Upon loading, slip events can be observed at a 45° angle with respect to the loading direction starting at approximately 1000 MPa. From EBSD crystallographic analysis (Fig. 6D), we correlate these slip events to partial dislocation nucleation from the free surface and subsequent stacking fault formation. Stacking fault formation occurs uniformly across the sample with no indication of twinning. After deforming plastically, the sample undergoes fracture at 2270 MPa. Fracture occurs perpendicular to the loading axis with no apparent necking. The post fracture image (Fig. 6C) shows thinner, rough edges on either side of the fracture surface.

4. Discussion

The Au bicrystals tested showed varying yield strengths ranging from 300 to 675 MPa with pronounced strain hardening in all samples. With respect to failure, the bicrystals exhibited either ductile failure upon twinning or sudden failure perpendicular to the loading direction. The GB may have higher strength in these thin film samples than in a bulk sample because dislocations can anneal at the free surfaces of the GB. To understand differences in mechanical behavior, we calculated the elastic modulus, Schmid factor, and relative GB energy for all samples (Table 1). From EBSD, we determined the crystallographic orientation of each grain in a bicrystal and subsequently determine the elastic modulus of the bicrystal using Eq. 1:

$$\frac{1}{E_{Bicrystal}} = \frac{1}{E_{Grain\ 1}} + \frac{1}{E_{Grain\ 2}} \tag{1}$$

Since the fabrication process of both the single crystal and bicrystal samples is similar, the in-plane and normal crystallographic orientations are also similar (Figs. 1F, 5, & 6). Thus, the elastic moduli and Schmid factors are similar across all the bicrys-

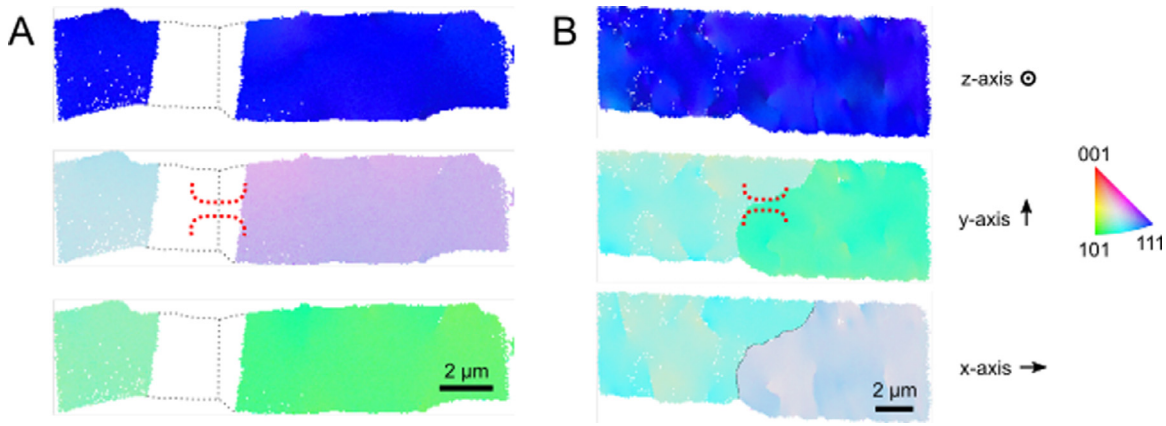

Fig. 5. EBSD orientation maps of bicrystals corresponding to the 56° GB (A) and 25° GB (B) in Fig. 4. The blank region in A is due to an oxide particle on the chip that obstructed the EBSD detector. The approximate location of the dog-bone shaped testing area is overlaid on the EBSD image with red dashed lines.

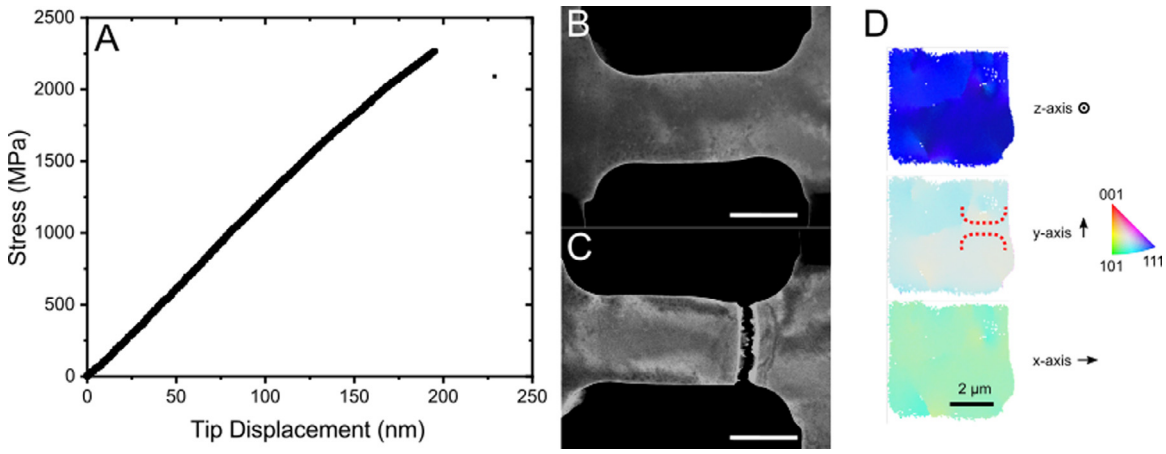

Fig. 6. A) Stress-displacement curve from a tensile test performed on a gold single crystal and the corresponding STEM images before (B) and after (C) the tensile test. The contrast in C is increased to see stacking faults, which are streaks of dark contrast. Scale bar is 500 nm. D) EBSD orientation maps of the single crystal. The approximate location of the dog-bone shaped testing area is overlaid on the EBSD image with red dashed lines.

Table 1
Material properties of single crystal and bicrystal samples. Elastic modulus values were determined from crystallographic data collected from EBSD and are not based on the experimental tests. Elastic modulus is not accurately measured in the experimental tests due to the lack of fiducial markers. Schmid factor calculations are for 1/6<211> partial dislocations. The GB energy is reported relative to the surface energy [41].

	Calculated Elastic Modulus (GPa)	Max Schmid Factor	Yield strength (MPa)	Critical resolved shear stress (MPa)	$\gamma_{GB}/\gamma_{surface}$
SC	77.4	0.49	1000	490	
25°	83.0	0.50	650	325	0.80
35°	80.2	0.48	300	144	0.93
56°	80.8	0.49	675	331	0.75

tal samples and the single crystal sample and cannot explain the differences in plastic behavior. The calculated critical resolved shear stress (CRSS) is approximately half of the yield stress in all cases. The SC sample has the highest CRSS, and the 35° bicrystal has the lowest CRSS.

Density functional theory has been used to calculate the tensile strength of specific grain boundaries in Al, W and SiC [43–45]. The strengths are on the order of ~10 GPa, close to theoretical strength values. Our samples fail far below these values. The tensile strength of the specific grain boundaries in the Au bicrystals are not available in the literature. Thus, we use GB energy as a related parameter. GB energies vary across the three bicrystal samples. The relative GB energy is calculated from the GB groove angles from an aggregated set of bicrystal data, which is described in greater detail in [41]. While GB energy generally increases with increasing misorientation angle, symmetries exist at specific angles due to lattice coherency of adjacent grains, which can lower GB energy. The 56° bicrystal has the lowest GB energy since it is close to the Σ3 twin GB angle of 60°. The 35° bicrystal has the highest GB energy and is close to a Σ7 GB. This is the only sample that failed through twinning, which indicates that GB energy may be correlated with failure mode, although a mechanistic reason for this remains unclear.

From Fig. 3, it appears that dislocation nucleation from the free surface is the primary driver of plasticity. Yield can occur when partial dislocations are nucleated at either the edge of the sample or at a dimple on the face of the sample. The critical resolved yield strengths for the bicrystals are within the range previously reported for compression tests of single crystal Au micropillars of similar size [46–49], whereas the yield stress of the single crystal sample is a factor of 1.5-2x larger and comparable to defect free, 150 nm wide <110> Au NWs [50]. The 25° and 56° bicrys-

tals (Fig. 4) and the single crystal sample fail in the same manner, which indicates that they should have similar yield strength, yet the single crystal yield strength is significantly higher. We attribute the large difference in yield strength between the single crystal and bicrystal samples to subtle differences on the surface of the samples that lead to differences in dislocation nucleation energy [51–54], and assume that yield occurs through dislocation nucleation at surfaces. This is also responsible for the scatter in the yield strengths of the bicrystal samples.

Strain hardening within single crystal and polycrystalline Au thin films has been correlated to high defect concentration that impedes dislocation motion [35], and extensive twinning [34]. In contrast, defect free Au NWs tested in tension plastically deform without strain hardening, since the likelihood of interactions between two mobile dislocations is unlikely in nanoscale samples [50,53,55–57]. The strain hardening observed in this work is similar to that observed previously in Au thin films. Compression tests on bicrystals nanopillars of less than 1 μm in size have shown that GBs act as dislocation sinks, thus preventing dislocation pileup [25,26]. This matches our observations from Fig. 3 and Movie S2 where most dislocations are absorbed at the GB or the free surfaces with no dislocation transmission. The low defect content, lack of multiple twins, and no dislocation pileup in our samples indicate that a different mechanism is responsible for strain hardening. We attribute the strain hardening observed to stacking fault-dislocation interactions away from the grain boundaries. This has been previously observed in nanocrystalline fcc metals and thin walled nanostructures [58,59]. Stacking fault-dislocation interactions were observed in Fig. 3C. Partial dislocations that nucleated from the edge of one grain intersected with partial dislocations that nucleated from the opposite side of the grain. This is observed as intersecting lines of contrast. This may also be the source of the subtler strain hardening observed in the single crystal sample above 1000 MPa.

As with yield strength, the fracture strength of the bicrystals is surprisingly lower than the single crystal sample. Yet, it is logical that the lower yield strengths of the bicrystals would lead to lower fracture strengths than in the single crystal, if the same deformation mechanisms lead to failure in both types of sample. Although the 25° and 35° bicrystals did fail at the edge of the GB (Fig. 4), none of the bicrystals fail along the GB. This is despite the fact that the GB is perpendicular to the loading direction for the 35° and 25° bicrystals, which favors failure along the GB and prevents GB slip. This indicates that the edge of the GB is a stress concentration [60], but that the GB itself is strong. Out-of-plane grooving at the GB may also serve as a stress concentration that is not visible in the TEM images. In the 25° and 56° bicrystals, the curved region at the base of the gauge length serves as a stress concentration that leads to failure. The absence of fracture at a pre-existing GB in bicrystal samples is in contrast to previous tensile studies of bulk Ni_3Al and Cu bicrystals with high GB energies that show brittle failure along the GB [16,61]. In nanocrystalline Au thin films tested in tension, dislocation-mediated GB sliding leads to void nucleation at GBs, which ultimately leads to intergranular fracture [60,62]. Even for the 25° bicrystal sample where there is a shear component acting along the GB (Fig. 4E & Movie S4), there is no GB sliding. Thus, we conclude that the GB orientation relative to the loading direction does not plays an important role in the failure behavior in these bicrystal samples.

The failure behavior of two of the bicrystals (Fig. 4) and the single crystal (Fig. 6) indicate a common mechanism that is not dependent on the presence of the GB. When compared to the only bicrystal sample, which exhibited ductile failure (Fig. 3), it is apparent that twinning promotes ductile failure. This behavior matches well with single crystal <110> Au NWs and thin films, where twinning occurred before necking and ductile failure [50,53,55–57,63]. In the samples that do not fail through twinning, the sudden fracture perpendicular to the loading axis, jagged edges on the fracture surface (Figs. 4 & 6), and lack of void formation are indicative of plastic collapse whereby the material fails via gross plasticity [64]. Plastic collapse is typically seen in materials under large stress with plastic zones that traverse the critical length scale of the material, such as foams [65–67], thin walled vessels [68–70], and more uncommonly thin films [64,71,72]. Plastic collapse is less likely along GBs since they act as efficient defect sinks for both dislocations and point defects [73,74]. This is supported by the lack of crack formation during tensile testing for all samples. From a fracture toughness analysis, the critical flaw size needed for crack propagation is larger than the dimensions of the microscale sample [75]. Thus, the samples do not undergo crack-mediated brittle fracture.

5. Conclusion

In summary, *in situ* TEM tensile testing is performed on Au bicrystal dog-bones with various misorientation angles, as well as a single crystalline sample. Yield strengths of the bicrystal samples matches with single crystal Au micropillar studies whereas the pronounced strain hardening observed is attributed to GB-dislocations interactions and stacking fault-dislocation interactions. In contrast to bulk bicrystal studies, failure does not occur at pre-existing GBs for any of the misorientation angles investigated. Rather, in the absence of twin formation or pre-existing flaws, failure occurs via plastic collapse for both bicrystal and single crystal samples. These results suggest that GBs are inherently strong and previously observed intergranular fracture in thin film samples is not directly related to GB energy.

Declaration of Competing Interest

The authors declare that they have no known competing financial interests or personal relationships that could have appeared to influence the work reported in this paper.

Acknowledgments

The authors thank Jim Ciston and Rohan Dall for their contributions to the TEM experiments and William D. Nix for the mechanical testing discussions. M.T.K. acknowledges the National Defense Science and Engineering Graduate Fellowship. M.T.K. and X.W.G. acknowledge the grant DE-SC0021075 funded by the U.S. Department of Energy, Office of Science, which supported the bicrystal in-situ TEM mechanical testing. L.T.G., R.T., R.Y., and J.A.F. acknowledge support from the NSF under Award 1804224, the Air Force Office of Scientific Research Multidisciplinary University Research Initiative under Award FA9550-16-1-0031, and the Packard Fellowship Foundation. Part of this work was performed at the Stanford Nano Shared Facilities (SNSF), which is supported by the National Science Foundation under award ECCS-1542152. Work at the Molecular Foundry was supported by the Office of Science, Office of Basic Energy Sciences, of the U.S. Department of Energy under Contract No. DE-AC02-05CH11231. The Division of Materials Science and Engineering, Office of Basic Energy Sciences, U.S. Department of Energy fully supported the time of C.M.B. and K.H. This work was performed, in part, at the Center for Integrated Nanotechnologies, an Office of Science User Facility operated for the U.S. Department of Energy (DOE) Office of Science. Sandia National Laboratories is a multimission laboratory managed and operated by National Technology & Engineering Solutions of Sandia, LLC, a wholly owned subsidiary of Honeywell International, Inc., for the U.S. DOE's National Nuclear Security Administration under contract DE-NA-0003525.

Supplementary materials

Supplementary material associated with this article can be found, in the online version, at doi:10.1016/j.actamat.2021.117505.

References

[1] J.J. Möller, E. Bitzek, Fracture toughness and bond trapping of grain boundary cracks, Acta Mater. 73 (2014) 1–11.
[2] P. Peralta, R. Dickerson, N. Dellan, K. Komandur, M.A. Jameel, Effects of local grain orientation on fatigue crack growth in multicrystalline fcc metallic materials, J. Eng. Mater. Technol. Trans. ASME. 127 (2005) 23–32.
[3] T. Watanabe, The impact of grain boundary character distribution on fracture in polycrystals, Mater. Sci. Eng. A. 176 (1994) 39–49.
[4] R.W. Armstrong, Material grain size and crack size influences on cleavage fracturing, Philos. Trans. R. Soc. A Math. Phys. Eng. Sci. 373 (2015).
[5] A. Das, Grain boundary engineering: fatigue fracture, Philos. Mag. 97 (2017) 867–916.
[6] T. Watanabe, P.W. Davies, Grain boundary sliding and intergranular fracture behaviour of copper bicrystals, Philos. Mag. A Phys. Condens. Matter, Struct. Defects Mech. Prop. 37 (1978) 649–681.
[7] Z.H. Aitken, D. Jang, C.R. Weinberger, J.R. Greer, Grain Boundary Sliding in Aluminum Nano-Bi-Crystals Deformed at Room Temperature, Small 10 (2014) 100–108.
[8] R.H. Kraft, J.F. Molinari, A statistical investigation of the effects of grain boundary properties on transgranular fracture, Acta Mater 56 (2008) 4739–4749.
[9] W.L. Li, J.C.M. Li, W.L. Li, The effect of grain size on fracture toughness, Philos. Mag. A Phys. Condens. Matter, Struct. Defects Mech. Prop. 59 (1989) 1245–1261.
[10] A. Pineau, A.A. Benzerga, T. Pardoen, Failure of metals I: Brittle and ductile fracture, Acta Mater 107 (2016) 424–483.
[11] J.R. Rice, R. Thomson, Ductile versus brittle behaviour of crystals, Philos. Mag. A. 29 (1974) 73–97.
[12] B.B. Rath, I.M. Bernstein, The relation between grain-boundary orientation and intergranular cracking, Metall. Trans. 2 (1971) 2845–2851.
[13] M.D. Sangid, T. Ezaz, H. Sehitoglu, I.M. Robertson, Energy of slip transmission and nucleation at grain boundaries, Acta Mater. 59 (2011) 283–296.
[14] J. Kacher, B.P. Eftink, B. Cui, I.M. Robertson, Dislocation interactions with grain boundaries, Curr. Opin. Solid State Mater. Sci. 18 (2014) 227–243.
[15] D.E. Spearot, M.A. Tschopp, K.I. Jacob, D.L. McDowell, Tensile strength of ⟨1 0 0⟩ and ⟨1 1 0⟩ tilt bicrystal copper interfaces, Acta Mater. 55 (2007) 705–714.
[16] J.Q. Su, M. Demura, T. Hirano, Grain-boundary fracture strength in Ni3Al bicrystals, Philos. Mag. A Phys. Condens. Matter, Struct. Defects Mech. Prop. 82 (2002) 1541–1557.
[17] Z.F. Zhang, Z.G. Wang, Dependence of intergranular fatigue cracking on the interactions of persistent slip bands with grain boundaries, Acta Mater. 51 (2003) 347–364.
[18] J.B. Brosse, R. Fillit, M. Biscondi, Intrinsic intergranular brittleness of molybdenum, Scr. Metall. 15 (1981) 619–623.
[19] H. Kurishita, A. Oishi, H. Kubo, H. Yoshinaga, Grain Boundary Fracture in Molybdenum Bicrystals with Various <110>Symmetric Tilt Boundaries, Trans. Japan Inst. Met. 26 (1985) 341–352.
[20] P.J. Imrich, C. Kirchlechner, C. Motz, G. Dehm, Differences in deformation behavior of bicrystalline Cu micropillars containing a twin boundary or a large-angle grain boundary, Acta Mater. 73 (2014) 240–250.
[21] C.S. Kaira, S.S. Singh, A. Kirubanandham, N. Chawla, Microscale deformation behavior of bicrystal boundaries in pure tin (Sn) using micropillar compression, Acta Mater. 120 (2016) 56–67.
[22] X. Zhang, S. Lu, B. Zhang, X. Tian, Q. Kan, G. Kang, Dislocation–grain boundary interaction-based discrete dislocation dynamics modeling and its application to bicrystals with different misorientations, Acta Mater. 202 (2021) 88–98.
[23] K.S. Ng, A.H.W. Ngan, Deformation of micron-sized aluminium bi-crystal pillars, Philos. Mag. 89 (2009) 3013–3026.
[24] L.L. Li, Z.J. Zhang, J. Tan, C.B. Jiang, R.T. Qu, P. Zhang, J.B. Yang, Z.F. Zhang, Stepwise work hardening induced by individual grain boundary in Cu bicrystal micropillars, Sci. Rep. 5 (2015) 1–8.
[25] Y. Kim, S. Lee, J.B. Jeon, Y.J. Kim, B.J. Lee, S.H. Oh, S.M. Han, Effect of a high angle grain boundary on deformation behavior of Al nanopillars, Scr. Mater. 107 (2015) 5–9.
[26] A. Kunz, S. Pathak, J.R. Greer, Size effects in Al nanopillars: single crystalline vs. bicrystalline, Acta Mater. 59 (2011) 4416–4424.
[27] N.V. Malyar, J.S. Micha, G. Dehm, C. Kirchlechner, Size effect in bi-crystalline micropillars with a penetrable high angle grain boundary, Acta Mater. 129 (2017) 312–320.
[28] N. Kheradmand, H. Vehoff, Orientation gradients at boundaries in micron-sized bicrystals, Adv. Eng. Mater. 14 (2012) 153–161.
[29] R. Ramachandramoorthy, W. Gao, R. Bernal, H. Espinosa, High Strain Rate Tensile Testing of Silver Nanowires: Rate-Dependent Brittle-to-Ductile Transition, Nano Lett. 16 (2016) 255–263.
[30] Y. Sun, B. Gates, B. Mayers, Y. Xia, Crystalline Silver Nanowires by Soft Solution Processing, Nano Lett. 2 (2002) 165–168.
[31] G. Richter, K. Hillerich, D.S. Gianola, R. Mönig, O. Kraft, C.A. Volkert, Ultrahigh Strength Single Crystalline Nanowhiskers Grown by Physical Vapor Deposition, Nano Lett. 9 (2009) 3048–3052.
[32] R.D. Emery, G.L. Povirk, Tensile behavior of free-standing gold films. Part II. Fine-grained films, Acta Mater. 51 (2003) 2079–2087.
[33] H.D. Espinosa, B.C. Prorok, Size effects on the mechanical behavior of gold thin films, J. Mater. Sci. 38 (2003) 4125–4128.
[34] A. Catlin, W.P. Walker, Mechanical properties of thin single-crystal gold films, J. Appl. Phys. 31 (1960) 2135–2139.
[35] C.A. Neugebauer, Tensile properties of thin, evaporated gold films, J. Appl. Phys. 31 (1960) 1096–1101.
[36] M.A. Haque, M.T.A. Saif, Deformation mechanisms in free-standing nanoscale thin films: a quantitative in situ transmission electron microscope study, Proc. Natl. Acad. Sci. U.S.A. 101 (2004) 6335–6340.
[37] G.D. Sim, J.J. Vlassak, High-temperature tensile behavior of freestanding Au thin films, Scr. Mater. 75 (2014) 34–37.
[38] K. Jonnalagadda, N. Karanjgaokar, I. Chasiotis, J. Chee, D. Peroulis, Strain rate sensitivity of nanocrystalline Au films at room temperature, Acta Mater. 58 (2010) 4674–4684.
[39] N.J. Karanjgaokar, C.S. Oh, J. Lambros, I. Chasiotis, Inelastic deformation of nanocrystalline Au thin films as a function of temperature and strain rate, Acta Mater. 60 (2012) 5352–5361.
[40] G. Dehm, Miniaturized single-crystalline fcc metals deformed in tension: New insights in size-dependent plasticity, Prog. Mater. Sci. 54 (2009) 664–688.
[41] L.T. Gan, R. Yang, R. Traylor, W. Cai, W.D. Nix, J.A. Fan, High-Throughput Growth of Microscale Gold Bicrystals for Single-Grain-Boundary Studies, Adv. Mater. 31 (2019) 1902189.
[42] C.I. Evans, R. Yang, L.T. Gan, M. Abbasi, X. Wang, R. Traylor, J.A. Fan, D. Natelson, Thermoelectric response from grain boundaries and lattice distortions in crystalline gold devices, Proc. Natl. Acad. Sci. U.S.A. 117 (2020) 23350–23355.
[43] G.-H. Lu, S. Deng, T. Wang, M. Kohyama, R. Yamamoto, Theoretical tensile strength of an Al grain boundary, Phys. Rev. B. 69 (2004) 134106.
[44] X. Wu, Y.W. You, X.S. Kong, J.L. Chen, G.N. Luo, G.H. Lu, C.S. Liu, Z. Wang, First-principles determination of grain boundary strengthening in tungsten: dependence on grain boundary structure and metallic radius of solute, Acta Mater. 120 (2016) 315–326.
[45] M. Kohyama, Tensile strength and fracture of a tilt grain boundary in cubic SiC: A first-principles study, Philos. Mag. Lett. 79 (1999) 659–672.
[46] C.A. Volkert, E.T. Lilleodden, Size effects in the deformation of sub-micron Au columns, Philos. Mag. 86 (2006) 5567–5579.
[47] S.-W.W. Lee, S.M. Han, W.D. Nix, Uniaxial compression of fcc Au nanopillars on an MgO substrate: The effects of prestraining and annealing, Acta Mater. 57 (2009) 4404–4415.
[48] R. Dou, B. Derby, A universal scaling law for the strength of metal micropillars and nanowires, Scr. Mater. 61 (2009) 524–527.
[49] S.-W. Lee, W.D. Nix, Size dependence of the yield strength of fcc and bcc metallic micropillars with diameters of a few micrometers, Philos. Mag. 92 (2012) 1238–1260.
[50] J.-H. Seo, H.S. Park, Y. Yoo, T.-Y. Seong, J. Li, J.-P. Ahn, B. Kim, I.-S. Choi, Origin of Size Dependency in Coherent-Twin-Propagation-Mediated Tensile Deformation of Noble Metal Nanowires, Nano Lett. 13 (2013) 5112–5116.
[51] H. Bei, S. Shim, M.K. Miller, G.M. Pharr, E.P. George, Effects of focused ion beam milling on the nanomechanical behavior of a molybdenum-alloy single crystal, Appl. Phys. Lett. 91 (2007) 111915.
[52] T. Zhu, J. Li, A. Samanta, A. Leach, K. Gall, Temperature and Strain-Rate Dependence of Surface Dislocation Nucleation, Phys. Rev. Lett. 100 (2008) 025502.
[53] J. Shin, L.Y. Chen, U.T. Sanli, G. Richter, S. Labat, M.-I.I. Richard, T. Cornelius, O. Thomas, D.S. Gianola, Controlling dislocation nucleation-mediated plasticity in nanostructures via surface modification, Acta Mater. 166 (2019) 572–586.
[54] Q.-J. Li, B. Xu, S. Hara, J. Li, E. Ma, Sample-size-dependent surface dislocation nucleation in nanoscale crystals, Acta Mater. 145 (2018) 19–29.
[55] A. Sedlmayr, E. Bitzek, D.S. Gianola, G. Richter, R. Mönig, O. Kraft, Existence of two twinning-mediated plastic deformation modes in Au nanowhiskers, Acta Mater. 60 (2012) 3985–3993.
[56] J.-H. Seo, Y. Yoo, N.-Y. Park, S.-W. Yoon, H. Lee, S. Han, S.-W. Lee, T.-Y. Seong, S.-C. Lee, K.-B. Lee, P.-R. Cha, H.S. Park, B. Kim, J.-P. Ahn, Superplastic Deformation of Defect-Free Au Nanowires via Coherent Twin Propagation, Nano Lett. 11 (2011) 3499–3502.
[57] Z. Xie, J. Shin, J. Renner, A. Prakash, D.S. Gianola, E. Bitzek, Origins of strengthening and failure in twinned Au nanowires: Insights from in−situ experiments and atomistic simulations, Acta Mater. 187 (2020) 166–175.
[58] Z. Yan, Y. Lin, Dislocation-stacking fault interactions in a nanostructured Al alloy processed by severe plastic deformation, Mater. Sci. Eng. A. 734 (2018) 224–228.
[59] R.P. Patil, D. Doan, Z.H. Aitken, S. Chen, M.T. Kiani, C.M. Barr, K. Hattar, Y.W. Zhang, X.W. Gu, Hardening in Au-Ag nanoboxes from stacking fault-dislocation interactions, Nat. Commun. 11 (2020) 1–9.
[60] E. Hosseinian, S. Gupta, O.N. Pierron, M. Legros, Size effects on intergranular crack growth mechanisms in ultrathin nanocrystalline gold free-standing films, Acta Mater. 143 (2018) 77–87.
[61] A. Vinogradov, S. Hashimoto, S. Miura, Crack propagation in ⟨110⟩ oriented copper bicrystals with the Σ9 and random boundary, Scr. Metall. Mater. 32 (1995) 427–431.
[62] E. Hosseinian, M. Legros, O.N. Pierron, Quantifying and observing viscoplasticity at the nanoscale: Highly localized deformation mechanisms in ultrathin nanocrystalline gold films, Nanoscale 8 (2016) 9234–9244.
[63] H.G.F. Wilsdorf, The role of glide and twinning in the final separation of ruptured gold crystals, Acta Metall. 30 (1982) 1247–1258.

[64] W.R. Lanning, S.S. Javaid, C.L. Muhlstein, Reconciling fracture toughness parameter contradictions in thin ductile metal sheets, Fatigue Fract. Eng. Mater. Struct. 40 (2017) 1809–1824.
[65] I. Jeon, T. Asahina, K.J. Kang, S. Im, T.J. Lu, Finite element simulation of the plastic collapse of closed-cell aluminum foams with X-ray computed tomography, Mech. Mater. 42 (2010) 227–236.
[66] C. Chen, A.M. Harte, N.A. Fleck, Plastic collapse of sandwich beams with a metallic foam core, Int. J. Mech. Sci. 43 (2001) 1483–1506.
[67] Y. Mu, G. Yao, L. Liang, H. Luo, G. Zu, Deformation mechanisms of closed-cell aluminum foam in compression, Scr. Mater. 63 (2010) 629–632.
[68] A. Robertson, H. Li, D. Mackenzie, Plastic collapse of pipe bends under combined internal pressure and in-plane bending, Int. J. Press. Vessel. Pip. 82 (2005) 407–416.
[69] M. Muscat, D. Mackenzie, R. Hamilton, A work criterion for plastic collapse, Int. J. Press. Vessel. Pip. 80 (2003) 49–58.
[70] X.K. Zhu, B.N. Leis, Average shear stress yield criterion and its application to plastic collapse analysis of pipelines, Int. J. Press. Vessel. Pip. 83 (2006) 663–671.
[71] M. Huang, Z. Suo, Q. Ma, Metal film crawling in interconnect structures caused by cyclic temperatures, Acta Mater. 49 (2001) 3039–3049.
[72] M. Ghidelli, S. Gravier, J.J. Blandin, P. Djemia, F. Mompiou, G. Abadias, J.P. Raskin, T. Pardoen, Extrinsic mechanical size effects in thin ZrNi metallic glass films, Acta Mater. 90 (2015) 232–241.
[73] M.W. Grabski, R. Korski, Grain boundaries as sinks for dislocations, Philos. Mag. 22 (1970) 707–715.
[74] C. Jiang, N. Swaminathan, J. Deng, D. Morgan, I. Szlufarska, Effect of grain boundary stresses on sink strength, Mater. Res. Lett. 2 (2014) 100–106.
[75] E.I. Preiß, B. Merle, M. Göken, Understanding the extremely low fracture toughness of freestanding gold thin films by in-situ bulge testing in an AFM, Mater. Sci. Eng. A. 691 (2017) 218–225.